



Contents lists available at ScienceDirect

International Journal of Plasticity

journal homepage: www.elsevier.com/locate/ijplas



Time-resolved evolution of the deformation mechanisms in a TRIP/TWIP Fe₅₀Mn₃₀Co₁₀Cr₁₀ high entropy during tensile loading probed with synchrotron X-ray diffraction

J.G. Lopes ^{a,*}, J. Shen ^{a,b}, E. Maawad ^c, P. Agrawal ^{d,e}, N. Schell ^c, R.S. Mishra ^{d,e}, J. P. Oliveira ^{a,b,*}

^a UNIDEMI, Department of Mechanical and Industrial Engineering, NOVA School of Science and Technology, Universidade NOVA de Lisboa, Caparica 2829-516, Portugal

^b CENIMAT/I3N, Department of Materials Science, NOVA School of Science and Technology, Universidade NOVA de Lisboa 2829-516 Caparica, Portugal

^c Institute of Materials Physics, Helmholtz-Zentrum Hereon, Max-Planck-Str. 1, Geesthacht D21502, Germany

^d Advanced Materials and Manufacturing Processes Institute, University of North Texas, Denton, TX 76207, USA

^e Center for Friction Stir Processing, Department of Materials Science and Engineering, University of North Texas, Denton, TX 76207, USA



ARTICLE INFO

Keywords:

FeMnCoCr
High entropy alloys
Synchrotron X-ray diffraction
In-situ testing
TWIP
TRIP
strengthening mechanisms

ABSTRACT

The present research focuses on analyzing the deformation mechanisms associated with tensile loading of the Fe₅₀Mn₃₀Co₁₀Cr₁₀ high entropy alloy (HEA) using synchrotron x-ray diffraction (SXRD). This novel material is comprised by two major phases: γ -FCC and ϵ -HCP, where transformation induced plasticity (TRIP) effectively transforms the first into the latter, upon the application of an external stress. However, the presence of thermally stable ϵ -HCP prior to loading will also influence the deformation mechanism of the material during mechanical solicitation. As such, here we investigate the activation of different strain accommodation mechanisms and the consequent microstructural evolution. Four stages were identified in the mechanical response of this novel HEA, where the TRIP and the twinning induced plasticity (TWIP) deformation modes are the main events granting this HEA its outstanding properties. Such sequence of events allows to evidence the effectiveness of the collaboration between the transformative capability of the γ -FCC phase and the work hardening potential of the ϵ -HCP phase. This analysis is performed via quantitative and qualitative analysis of the SXRD data, allowing also to investigate the response behavior of specific crystallographic planes to the increasing stress throughout the experiment.

1. Introduction

Over the past few years, high entropy alloys (HEAs) have been a hot topic in the materials science realm. The premise on which they are based on is that of a multi-principal element configuration that grants a wide compositional space for the discovery of new materials with potentially interesting properties (George et al., 2019; Miracle and Senkov, 2017; Tang et al., 2023; Ye et al., 2016). In line with this, fine compositional tuning of these advanced alloys permits targeting of key mechanisms that are fundamental for specific engineering purposes. More specifically, these materials are candidates for structural applications, where other traditional metals, such

* Corresponding authors.

E-mail addresses: jeg.lopes@campus.fct.unl.pt (J.G. Lopes), jp.oliveira@fct.unl.pt (J.P. Oliveira).

as steels, have already been extensively researched to accomplish high performing tasks (Ding et al., 2011; Grässel et al., 2000; Magagnosc et al., 2021). Such structures can, thus, benefit from the activation of specific microstructural load bearing mechanisms, while benefiting from solid solution strengthening characteristic of HEAs. In this sense, these alloys can overcome ductility-strength trade off that remains a challenge amidst engineers to this day (Bahramyan et al., 2020; Hilhorst et al., 2023), while also showcasing high thermal stability allowing their use in more demanding applications.

In this regard, literature evidences that efforts are being made to develop and understand such advanced materials to meet modern-day structural requirements. For instances, Li et al. (Y.X. Li et al., 2023) reported on the tensile deformation behavior of an FCC-structured Fe₄₅Co₂₅Ni₁₀V₂₀ HEA, at a temperature of 77 K. Their results highlighted the material phase transformations, from an FCC to a BCC crystal structure, through stress concentration at grain boundaries and intersection of stacking faults. Such granted the analyzed HEA to benefit from strain accommodation achieved both during phase transition and further deformation of the BCC phase. In a different study, Kim et al. (2022) highlighted the temperature-dependent mechanical performance of the Fe₄₀Mn₄₀Co₁₀Cr₁₀ HEA, subjecting it to tensile testing at 223 and 298 K. While phase transition was also observed occurring from an FCC to an HCP crystal structure, deformation twinning also played an important role during deformation, remarking that stacking fault energy temperature dependence, led to the preference of deformation twining in detriment of phase transformation.

Following this line of thought, another relevant alloy is the dual-phase Fe₅₀Mn₃₀Co₁₀Cr₁₀ (DP-HEA), known for the existence of metastability between the γ -FCC and ϵ -HCP phases. This material, which can trigger the transformation induced plasticity (TRIP) and twinning induced plasticity (TWIP) effects upon mechanical loading has gathered increasing interest in the past few years (Hossain and Kumar, 2022; Kim et al., 2022; Li et al., 2017, 2016; Liu et al., 2021).

While TRIP effect relies on the non-spontaneous athermal martensitic transformation process occurring in the γ -FCC phase by means of plastic strain, the TWIP effect is related to the high stacking fault energy of a given phase, in this case the ϵ -HCP. Given this, in one hand, TRIP acts through the continuous increase in stress causes the gliding of Shockley partial dislocations, aligned with the 1/6 ⟨112⟩ Burgers vector, leading to the coalescence of stacking faults in the γ -FCC phase, thus causing the nucleation of ϵ -HCP amidst the γ -FCC grains (Lai et al., 2022; Sohrabi et al., 2023; Zhao et al., 2021). On the other hand, the TWIP effect is characterized as the tendency to generate twins as a reaction to external stresses, instead of forming stacking faults (Gui et al., 2022; Lai et al., 2022; Li et al., 2022). It is, therefore, the balance between these two phases, and their evolution, that will dictate the mechanical performance of the DP-HEA, including the several stages of deformation exhibited by it, upon tensile loading.

Delving onto this matter, several studies have been conducted to evaluate such DP-HEA performance under mechanical loading. For instance, Li et al. (Li et al., 2017) indicated that multiple deformation mechanisms and dynamic strain partitioning are exhibited by the DP-HEA. They indicated that the γ -FCC phase matrix accommodates the external plastic strain at early stages of deformation via TRIP, stacking faults and dislocation slip, while the ϵ -HCP phase acts at later stages of deformation via mechanical twinning, dislocation slip and formation of stacking faults, thus preventing premature failure. Similar findings were presented by Fu et al. (Fu et al., 2018) via in-situ time-of-flight neutron diffraction during tensile testing, where the crystallographic planes specific behavior was highlighted. Furthermore, the strain rate sensitivity of DP-HEA also has been investigated (Basu et al., 2018; He et al., 2020), where major changes on the deformation mechanisms were only found at high strain rates. Nevertheless, the most documented parameter affecting the deformation behavior on this HEA, with special emphasis on the dislocation slip, is the ϵ -HCP c/a ratio (Bu et al., 2019; Sinha et al., 2019), which governs over dislocation slip mode occurring in this phase.

Concerning all these results, the next logical step is to pinpoint the sequence of events and the stress level at which each strain accommodation mechanism is activated. Such mechanisms correspond to dislocation slip, twinning (via TWIP) and phase transformation (due to TRIP). In light of this matter, such can be investigated via in-situ tensile testing under synchrotron X-ray radiation. This time-resolved approach during mechanical loading, allows to detail diffraction peak specific reactions to the externally imposed stress and is, therefore, essential to understand how strain accommodation mechanisms are activated and interact with each other to sustain increasing levels of stress. Similar investigations, using in-situ synchrotron and neutron diffraction, have been taken by researchers with several other materials, including pure beryllium (Ferreri et al., 2022), steel (Li et al., 2023a; Magagnosc et al., 2021), Mg alloys (Abdolvand et al., 2015), titanium alloys (Ellyson et al., 2023) and even other HEA compositions (Rogachev et al., 2021; Shen et al., 2024, 2023). Nevertheless, different compositions render different microstructures, especially in what concerns the metastability of the ϵ -HCP phase. Thus, the resulting mechanical properties and different deformation mechanisms that can be activated during loading of these materials, must evaluated considering both composition, microstructure and thermomechanical processing (if any).

In this study, we delve deeper into the topic, in order to complement, verify and validate the mechanical response of the DP-HEA, using an in-situ tensile test synchrotron X-ray diffraction (SXRD) approach. This allows us to obtain a relevant view on the activation of the different strain accommodation mechanisms during tensile loading, correlating them with the evolution of both microstructure and mechanical properties. Such is performed by inferring upon the data obtained from characteristic diffraction peaks of each phase at specific orientation to gain also insights into the direction-specific evolution of microstructure and properties. This way, parameters like phase fraction, lattice strain, integrated intensity, c/a ratio and dislocation density can be analyzed with respect to the active deformation mechanisms and correlated to the different loading stages developed throughout the tensile test.

2. Materials and methods

2.1. In-situ tensile test under synchrotron X-ray diffraction

To acquire in-depth information about the mechanical response of the DP-HEA under tensile solicitation, in-situ SXRD

measurements were conducted in transmission mode using the P07B High Energy Materials Science beamline of PETRA III at the DESY synchrotron.

For such, a Fe₅₀Mn₃₀Co₁₀Cr₁₀ ingot was manufactured by melting and casting in a vacuum induction furnace, using pure metals as raw materials. The material was used in its as-cast condition, to assess the suitability for structure application without the need for further thermomechanical processing. Tensile specimens with a thickness of 1.5 mm, width of 1.5 mm and a gauge length of 29 mm, were then cut by wire electrical discharge machining. The oxide layer left by the process was removed with 1200 Grit sandpaper to reduce any potential influence of this layer on crack nucleation upon tensile loading. For observing the initial microstructure of the DP-HEA, and conduct grain size measurements, electron backscatter diffraction (EBSD) maps were obtained in a FEI Nova NanoSEM 230 equipped with a EDAX Hikari Super EBSD detector. Additionally, to complement this analysis, optical microscopy (OM) was also performed and is presented in Figure S.1 in the supplementary material along with description of the process.

Tensile tests were performed at room temperature and at a strain rate of 10^{-3} s^{-1} , being intermittently stopped for the acquisition of the raw experimental diffraction data at consecutive deformation stages. At each loading step the material was exposed to a $700 \times 700 \mu\text{m}^2$ high-energy photon beam (87.1 keV) for 0.1 s, and 10 diffraction images, as well as dark images, were captured. The diffracted beam was captured using a 2048×2048 pixel Perkin Elmer XRD 1622 detector (with a pixel size of 200 μm), approximately located 1.226 m from the tensile specimen. The sample-to-detector distance was determined using LaB₆ calibrant, which was also used to determine the broadening associated to the beamline optics.

The obtained stress-strain data, in the plastic regime, was then fitted following the modified Ludwigson model (Lavakumar et al., 2021), as described in the supplementary material. This was made to account for the TRIP or TWIP effects, which can have a distinctive behavior on the tensile response of the material (Clayton and Lloyd, 2021; Wong et al., 2016). The strain hardening rate was then computed as $d\sigma/d\varepsilon$, using the fitting parameters as input. Postmortem analysis of the fracture surface was performed using a Hitachi SU8000 scanning electron microscope (SEM).

2.2. Synchrotron data analysis

Using the pyFAI python package (Kieffer et al., 2020), the raw diffraction experimental data was converted from 2D diffraction images to 1D diffraction patterns. Conversion was performed by full integration along the azimuthal angle, φ , to obtain an overall understanding of the microstructure evolution of the analyzed HEA. Furthermore, to evaluate the orientation-dependent microstructure evolution 10° integrations along the loading direction, LD, and transverse direction, TD, obtained by integration within the 85 to 95° and -5 to +5° ranges, were performed (refer to Fig. 1). To assess the twinning activation on the ε-HCP phase caking using 1° segments was performed to evaluate the status of individual reflections at specific loading stages.

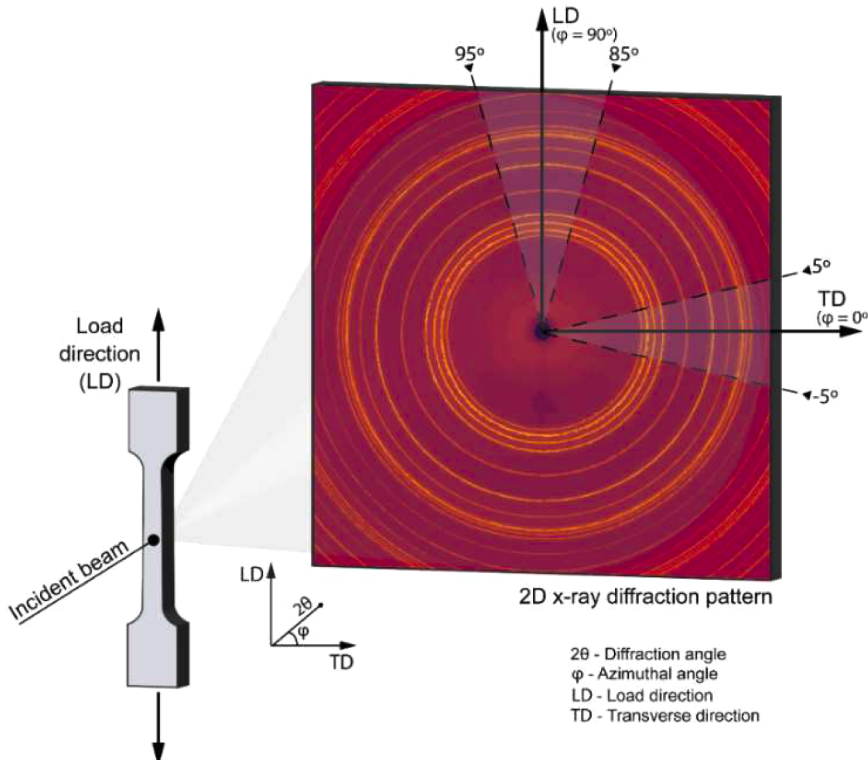


Fig. 1. Experimental setup (not to scale).

Due to the presence of two phases on this HEA, (partial) overlapping of the diffraction peaks was to be expected within the 2θ angle range of interest. Nevertheless, to acquire meaningful information, such as peak center, full width at half maximum (FWHM) and integrated peak intensity, the (1 0 -1 0), (0 0 0 2), (1 0 -1 1), (1 0 -1 2), (1 0 -1 3) and the (1 1 1), (2 0 0) and (3 1 1) phase reflections were selected to study the ϵ -HCP and the γ -FCC phases, respectively.

The diffraction peaks were fitted with a Voigt profile along with the neighboring background, using a Chebyshev polynomial (Wang et al., 2021; Zeng et al., 2021). The Voigt profile was chosen given its capability to accurately describe the peak shape, as the combined influence of both of its components, being described as the convolution of a Gaussian and Lorentzian functions (Langford, 1978).

Using Eq. (1), the lattice strain, ϵ_j^{hkl} , was computed from the 10° integration segments corresponding to LD and TD. d_j^{hkl} is the interplanar spacing corresponding to a given (h k l) phase reflection at a certain deformation stage, j. In this study, d_0^{hkl} is the interplanar spacing at the stress-free stage of the tensile test, i.e., without any applied load, following the same assumption made in (Magagnosc et al., 2021; Naeem et al., 2020), yielding a good approximation of the lattice strain imparted by each crystallographic plane during loading.

$$\epsilon_j^{hkl} = \frac{d_j^{hkl} - d_0^{hkl}}{d_0^{hkl}} \quad (1)$$

For the determination of d_j^{hkl} , Bragg's law (Equation 2) is of fundamental importance as it is a condition for constructive interference to occur, resulting in the existence of peaks on the diffraction pattern, correlating the interplanar spacing, d_j^{hkl} , with the 2θ value of the peak center of a given diffraction peak (He, 2018).

$$n \cdot \lambda = 2 \cdot d_j^{hkl} \cdot \sin(\theta_j^{hkl}) \quad (2)$$

here, λ is the X-ray beam wavelength, which is 0.14235 \AA , and θ_j^{hkl} corresponds to half of the peak center position, as obtained through fitting. Aside from these, the order of reflection, n, is a positive integer, which for the analyzed peaks equals to 1. When such law is not fulfilled, destructive interference takes place meaning that the diffracted beam will not be in phase with each other, and no phase reflection is observable. Linear fitting of the lattice strain in the LD (in the elastic regime) of each diffraction reflection allowed to obtain its corresponding Young's modulus.

Moreover, for calculation of the dislocation density (ρ), Equation 3 (Lin et al., 2015; Smallman and Westmacott, 1957) was employed, where the term $\langle \epsilon^2 \rangle$ corresponds to the microstrain, D is the crystallite size and b is the burgers vector.

$$\rho = \frac{2 \cdot \sqrt{3} \cdot \langle \epsilon^2 \rangle^{\frac{1}{2}}}{b \cdot D} \quad (3)$$

For the γ -FCC phase the magnitude of b is $\frac{\sqrt{2}}{2} \cdot a_\gamma$, where a_γ is the γ -FCC lattice constant (Shen et al., 2024). While for the ϵ -HCP phase, $b = 1/3$ (11–20) is utilized to quantify basal-type dislocations and $b = 1/3$ (11–23) to quantify prismatic-type dislocations, with their magnitude depending on their slip plane (Hull and Bacon, 2011).

By performing a linear fitting using the Halder-Wagner method (Lin et al., 2015; Verma et al., 2020), $\langle \epsilon^2 \rangle$ and D were computed. This method considers θ_j^{hkl} , $FWHM_j^{hkl}$ (after subtraction the instrumental broadening obtained from the LaB₆ powder standard diffraction data) and the factor K which is considered 4/3 for spherical crystallites, as in Eq. (4).

$$\frac{(FWHM_j^{hkl})^2}{\tan^2(\theta_j^{hkl})} = \frac{K \cdot \lambda}{D} \cdot \frac{FWHM_j^{hkl}}{\tan(\theta_j^{hkl}) \cdot \sin(\theta_j^{hkl})} + 16 \cdot \langle \epsilon^2 \rangle \quad (4)$$

This way the dislocation density for each dislocation mode was computed to account for the variation in burgers vector, due to the dynamic change in lattice parameters, while accounting for the evolution of the Halder-Wagner plot outputs throughout the tensile test.

Furthermore, calculation of lattice constants in the LD and TD was performed to compute the volume averaged lattice strain imparted by each phase. For the γ -FCC phase, the lattice constant, a, was obtained based on the intensity averaged contribution of each analyzed peak. In turn, the calculation of the ϵ -HCP lattice constants, a and c, was based on (1 0 -1 0) and (1 0 -1 3) peaks, which correspond to the softest and the hardest diffraction peaks analyzed within this phase. Then, the volume averaged lattice strain related to each individual lattice parameter was calculated using $\epsilon_{a,j} = (a_j - a_0) / a_0$ and $\epsilon_{c,j} = (c_j - c_0) / c_0$, where in the case of the ϵ -HCP phase the calculated strain values were averaged using $\epsilon_{\epsilon\text{-HCP},j} = (2 \cdot \epsilon_{a,j} + \epsilon_{c,j}) / 3$ (Erdely et al., 2018). Here, again, the index j denotes a certain deformation stage, while 0 denotes the stress-free condition. The obtained values were then utilized, via the Von Misses stress equation, to compute the stress contribution (σ_j^{ph}) associated to each phase throughout the full extension of the tensile test, as in Eq. (5) (Shen et al., 2023).

$$\sigma_j^{ph} = \frac{1}{\sqrt{2}} \cdot \left[(\sigma_{1,j} - \sigma_{2,j})^2 + (\sigma_{2,j} - \sigma_{3,j})^2 + (\sigma_{3,j} - \sigma_{1,j})^2 \right]^{\frac{1}{2}} \quad (5)$$

where, $\sigma_{1,j}$ is the principal stress aligned with LD and $\sigma_{2,j}$ and $\sigma_{3,j}$ are the principal stresses normal to it. The values for $\sigma_{1,j}$, $\sigma_{2,j}$ and $\sigma_{3,j}$, were calculated using the obtained lattice strain values, through Eq. (6), where $\varepsilon_{2,j}$ is assumed equal to $\varepsilon_{3,j}$ (Ma et al., 2017).

$$\sigma_{g,j}^{ph} = \frac{E_{ph}}{1 + \nu_{ph}} \cdot \varepsilon_{g,j} + \frac{E_{ph} \cdot \nu_{ph}}{(1 + \nu_{ph})(1 - 2 \cdot \nu_{ph})} \cdot (\varepsilon_{1,j} + \varepsilon_{2,j} + \varepsilon_{3,j}) \quad (6)$$

here, $\sigma_{g,j}^{ph}$ is the principal stress aligned in a principal direction, g, corresponding to each phase (ph) at a given loading stage, j. E_{ph} corresponds to the Young's modulus of each phase, which is obtained through linear fitting of the lattice strain vs stress in the LD within the elastic range, and the Poisson ratio (ν_{ph}) was calculated according to the formula $\nu_{ph} = - (E_{LD} / E_{TD})$. Finally, the weighted average contribution of each phase can be used to compute the total stress partaken by the DP-HEA, using the phase volume fraction of each phase ($V^{\gamma\text{-FCC}}$ and $V^{\epsilon\text{-HCP}}$) as weighting factors as in Eq. (7) (Peng et al., 2022).

$$\sigma = V_j^{\gamma\text{-FCC}} \cdot \sigma_j^{\gamma\text{-FCC}} + V_j^{\epsilon\text{-HCP}} \cdot \sigma_j^{\epsilon\text{-HCP}} \quad (7)$$

3. Results

3.1. Microstructure description throughout tensile loading

The initial microstructure condition and overall mechanical performance of the DP-HEA are presented in Fig. 2. Observing the data contained within the EBSD inverse pole figure (IPF) and phase maps present in Fig. 2a) and b), the dual phase nature of the DP-HEA is revealed, as the two phases characteristic of this HEA, austenite (γ -FCC) and martensite (ϵ -HCP) can be easily identified. From this technique and from the microscopy performed via OM, we can infer that the γ -FCC grains exhibit a polygonal shape, with an average grain size of $40.2 \pm 10.7 \mu\text{m}$, while plate-like ϵ -HCP grains can be observed amidst the DP-HEA microstructure. However, note that for EBSD and OM sample preparation, the plastic deformation and material removal processes involved in polishing may cause TRIP to

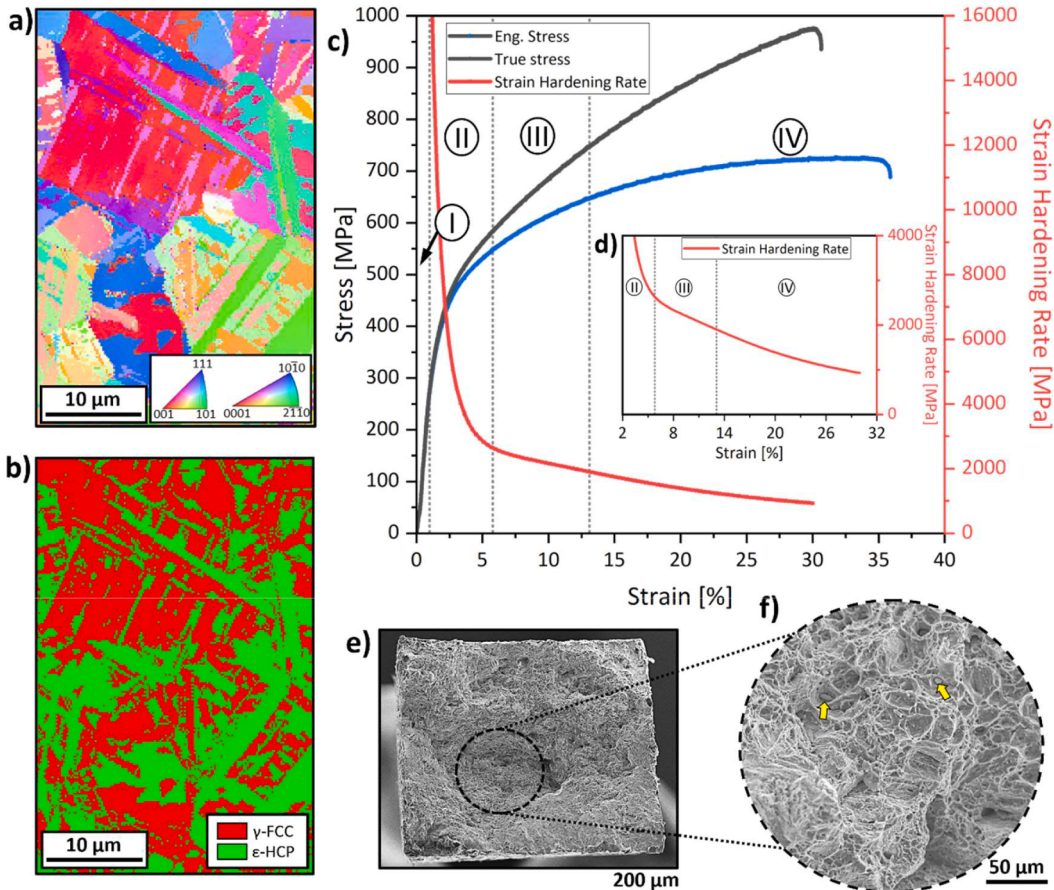


Fig. 2. Microstructure evaluation and mechanical behavior of the DP-HEA: a) EBSD IPF and b) EBSD phase maps; c) Engineering and true stress/strain curves describing the macroscopic tensile behavior of the DP-HEA, along with the strain hardening rate, which is further detailed in d); e) fracture surface and f) its corresponding detailed view.

occur at the surface, thus resulting in a slightly higher fraction of ϵ -HCP than that which is really present in the bulk of the material. Such, however, does not hinder the present discussion of the SXRD results, provided that not only do we work in transmission mode, as different samples, other than those used for EBSD and OM characterization, were tested during the experiment.

Furthermore, the engineering and true stress-strain curves of the material are also exhibited (refer to Fig. 2c). Upon loading the alloy entered the plastic regime at ≈ 319 MPa, reaching an ultimate tensile strength of 726 MPa and eventually fracturing at an elongation of 36 % (all engineering values). These results are comparable to those found in the literature regarding this HEA (Basu et al., 2018; Fu et al., 2018; He et al., 2020; Hossain and Kumar, 2022; Li et al., 2017), indicating its consistency with the data already available concerning the DP-HEA. However, it should be mentioned that the tensile properties of the DP-HEA are highly dependent on the initial ϵ -HCP phase volume fraction (Li et al., 2017). Thus, any (minor) differences between the tensile behavior obtained in present study and those found in the literature, can also be due to the intermittent loading process to which the sample was subjected during the in-situ tensile test to acquire the diffraction patterns at each loading stage.

Moreover, the strain hardening rate, calculated from the true stress-true strain data is displayed and further detailed in Fig. 2c) and d), respectively. From it we can identify four different stages within the tensile loading response of the DP-HEA. The first corresponds to the elastic portion of the curve, that ultimately ends with the onset plastic deformation. From that point on, a steep and continuous decrease with each increment of strain can be observed up to a true strain value of ≈ 6 %, marking the onset of new loading stage. Finally, when reaching a true-strain level of ≈ 13 %, the onset of a final loading stage can be marked. Although subtle, these changes occurring in the strain hardening rate account for the activation of the TRIP and TWIP effects. Such evidences that the DP-HEA becomes significantly stronger with the increasing loading and is going to be discussed further with the aid of diffraction data.

Eventually, upon failure, the fracture surface exhibited several dimples characteristic of a ductile-like fracture as observed via electron microscopy in Fig. 2(e) and (d). Also, the presence of scarcely scattered round particles can also be observed (marked with yellow arrows), corresponding to Mn oxides. These have also been identified in (Hossain and Kumar, 2022; Lopes et al., 2023a) and can be expected due to the high Mn content in the DP-HEA composition.

Considering this, we now turn our attention to the SXRD data results. In Fig. 3, we can observe the microstructural evolution (obtained after full azimuthal integration), of the DP-HEA upon loading on a crystal structure perspective. Starting with phase identification, we can observe that diffraction peaks corresponding to γ -FCC, ϵ -HCP and MnO phases are present, corroborating the previous observation using optical and electron microscopy. Note that the latter phase corresponds to lower intensity peaks that can only be properly observed by utilizing a logarithmic scale in the intensity axis due to the reduced volume fraction of MnO, which was

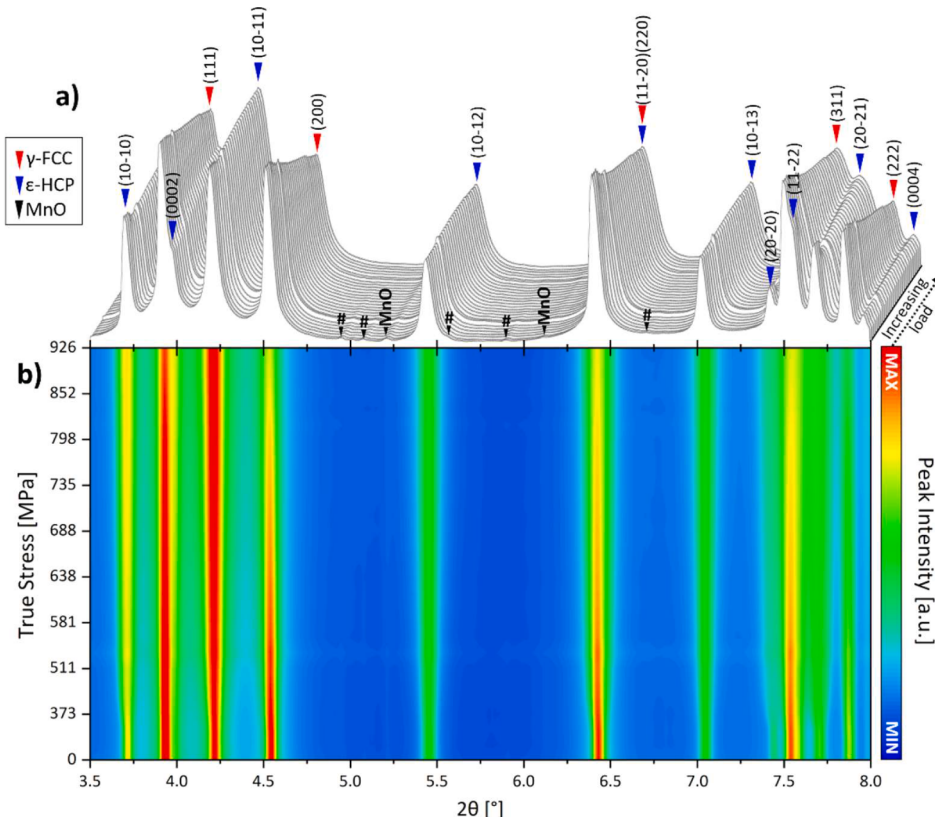


Fig. 3. a) Full azimuthal integration of the diffraction patterns obtained during tensile testing alongside with b) the corresponding colormap which evidences peak broadening and intensity changes with the increasing load (# corresponds to 2nd reflections).

determined to be $\approx 1\%$.

Additionally, evidencing the variation of peak intensity with increasing load, the colormap of Fig. 3(b)) highlights significant changes in the evolution of different diffraction peaks with each loading step. Given this, further single peak analysis of the diffraction data was conducted to gather a deeper understanding of the microstructural changes visible with SXRD.

Regarding this microstructural evolution occurring in the DP-HEA during tensile test, we start by addressing the effect of TRIP on the DP-HEA. For this, Fig. 4 highlights the continuously increasing ϵ -HCP phase fraction after the onset of TRIP, upon entering the plastic regime (at ≈ 250 MPa, which is the nearest point to the yield strength measured in Fig. 2c). From this data we can observe that prior to the tensile test the amount of ϵ -HCP on the DP-HEA was approximately of 33 % in volume fraction, reaching nearly 77 % upon fracture. It must also be emphasized that while TRIP is occurring, the mechanical behavior of the already deformed and newly formed ϵ -HCP phase in the alloy can be different (Sinha et al., 2019). However, it is not possible to separate the contributions of newly formed and thermally stable ϵ -HCP by synchrotron X-ray diffraction, thus the mechanical behavior of ϵ -HCP phase simultaneously considers those conditions. Given this, fluctuations on the amount of ϵ -HCP being formed throughout the tensile test can be observed and correlated with the evolution of the ϵ -HCP c/a ratio.

On this topic, the evolution of the lattice constants, which indicate the overall behavior of each phase, must first be mentioned. In the γ -FCC phase, the lattice constant, a , is 3.582 \AA at the beginning of the test, exhibiting a continuous increase, up to 3.588 \AA at the final loading stage. Such is coherent with the increase in interspatial distance due to the tensile loading. Additionally, in the ϵ -HCP case, the values of a and c are $\approx 2.535 \text{ \AA}$ and $\approx 4.100 \text{ \AA}$, respectively, prior to the experiment, whereas the value of a tends to increase and the value of c exhibits a decreasing tendency, reaching the values of $a \approx 2.540 \text{ \AA}$ and $c \approx 4.097 \text{ \AA}$.

Upon the onset of TRIP, the c/a ratio decreases drastically until the stress imparted by the material reaches ≈ 530 MPa, where it becomes stable. At this point a massive increase in the ϵ -HCP phase fraction can be observed, indicating that the initial strain accommodation mechanisms occurring in the both phases reached a critical stage, where the TRIP effect becomes more prominent, and stabilization of the ϵ -HCP phase lattice, due to the activation of different strain accommodation processes, acted together to prevent premature failure. However, when reaching ≈ 655 MPa, a sharp decrease on the c/a ratio can again be observed, marking the onset of a different stage on the mechanical behavior of the DP-HEA. These strain accommodation stages are responsible for the mechanical behavior of the DP-HEA and the following sections will illustrate the changes occurring on the diffraction peaks that take place at the onset of each stage.

3.2. Evolution of integrated peak intensity and ϵ -HCP twinning activation

To unveil the deformation mechanisms occurring considering different grain orientations, the integrated diffraction intensities were obtained from the LD and TD integrated data at each loading step. The results can be observed in Fig. 5.

Starting from the γ -FCC phase (refer to Fig. 5(a)), all integrated intensities of the analyzed diffraction reflections exhibit an overall similar trend. As it is possible to observe, before reaching the yield strength, the intensity (1 1 1) and (2 0 0) planes tend to increase

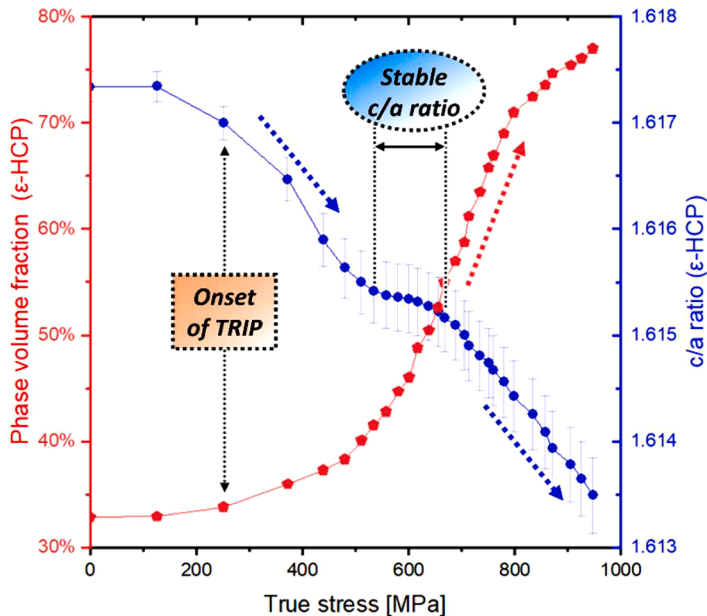
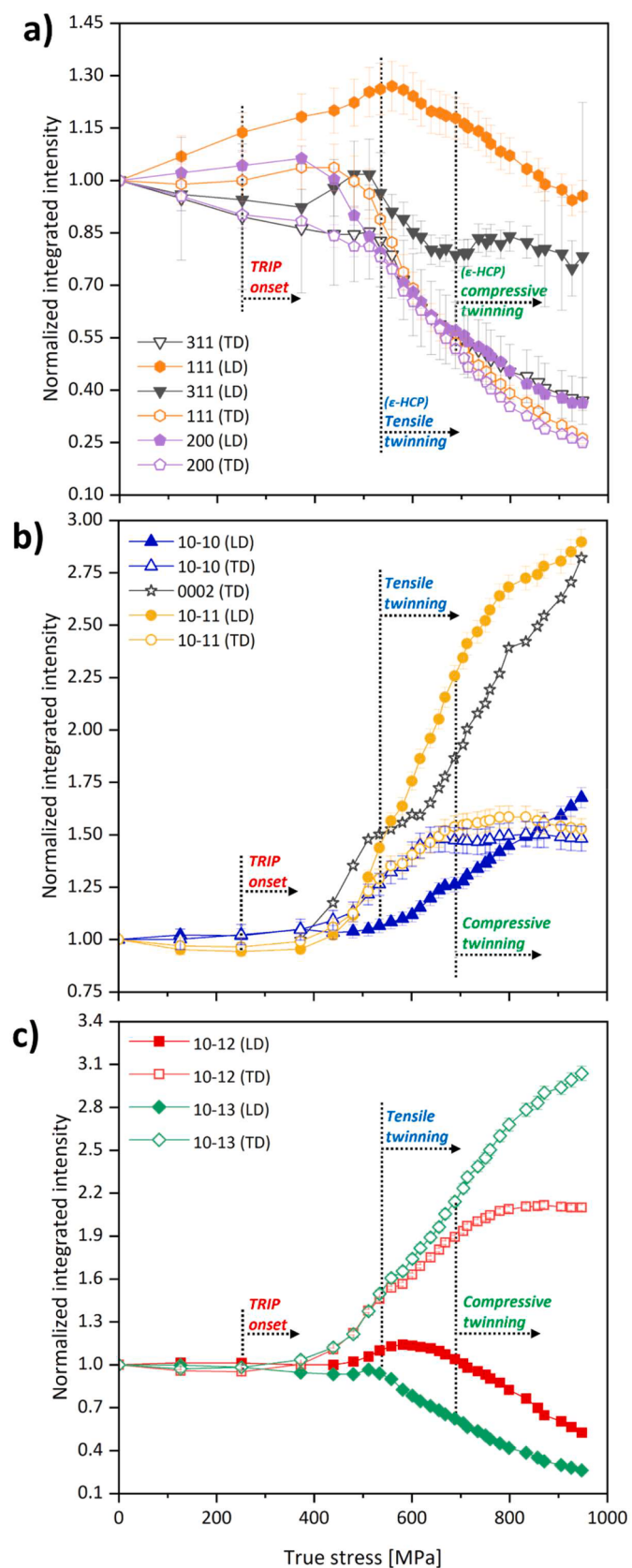


Fig. 4. Evolution of ϵ -HCP phase fraction obtained via Rietveld refinement (using MAUD (Saville et al., 2021)) with an R_{wp} below 5 % and c/a ratio evolution throughout the tensile test calculated using single peak analysis considering the (1 0 -1 0) and (1 0 -1 3) diffraction peaks, highlighting the variations occurring at the microstructural level on the DP-HEA.



(caption on next page)

Fig. 5. Normalized integrated intensity evolution during tensile test along TD and LD. (a) shows the evolution of γ -FCC (1 1 1), (2 0 0) and (3 1 1) diffraction peaks; (b) details the evolution of ϵ -HCP (1 0 -1 0) and (1 0 -1 1) diffraction peaks. Here, the (0 0 0 2) peak evolution is only shown for reference in the TD; (c) shows the evolution of ϵ -HCP (1 0 -1 2) and (1 0 -1 3) diffraction peaks.

aligned with the LD, while a slight decrease can be observed for the (3 1 1) peak in this direction. Interestingly, the (1 1 1) intensity shows the higher intensities aligning with the LD, which is coherent with the expected preferential deformation direction of FCC materials (Lopes et al., 2023b). This behavior continues to exhibit a stable behavior allowing for the γ -FCC grains to rotate, except for the (2 0 0) diffraction peaks, where upon the onset of TRIP, there is a major decrease in intensity in both directions.

Nevertheless, it is when reaching approximately a stress level of 530 MPa that the integrated intensity of all peaks evidences a sharp decrease. This agrees with the phase volume fraction results obtained from Rietveld refinement (refer to Fig. 4), meaning that at this stage the TRIP effect becomes more predominant, to relax the stresses imposed by tensile loading, within the γ -FCC rich microstructure.

Considering the peak intensity evolution of the ϵ -HCP phase, Fig. 5(b) and (c) displays the results obtained for the (1 0 -1 0), (1 0 -1 1), (1 0 -1 2) and (1 0 -1 3) diffracting reflections. Here, the intensity results for the (0 0 0 2) plane are also shown as a reference, as this reflection only starts being noticeable at the onset of plastic deformation exhibiting an ascendant behavior on the TD and being practically non-existent on the LD (this being the reason on why this is not shown). Such behavior can be associated with the TRIP effect, as it effectively transforms the γ -FCC into ϵ -HCP.

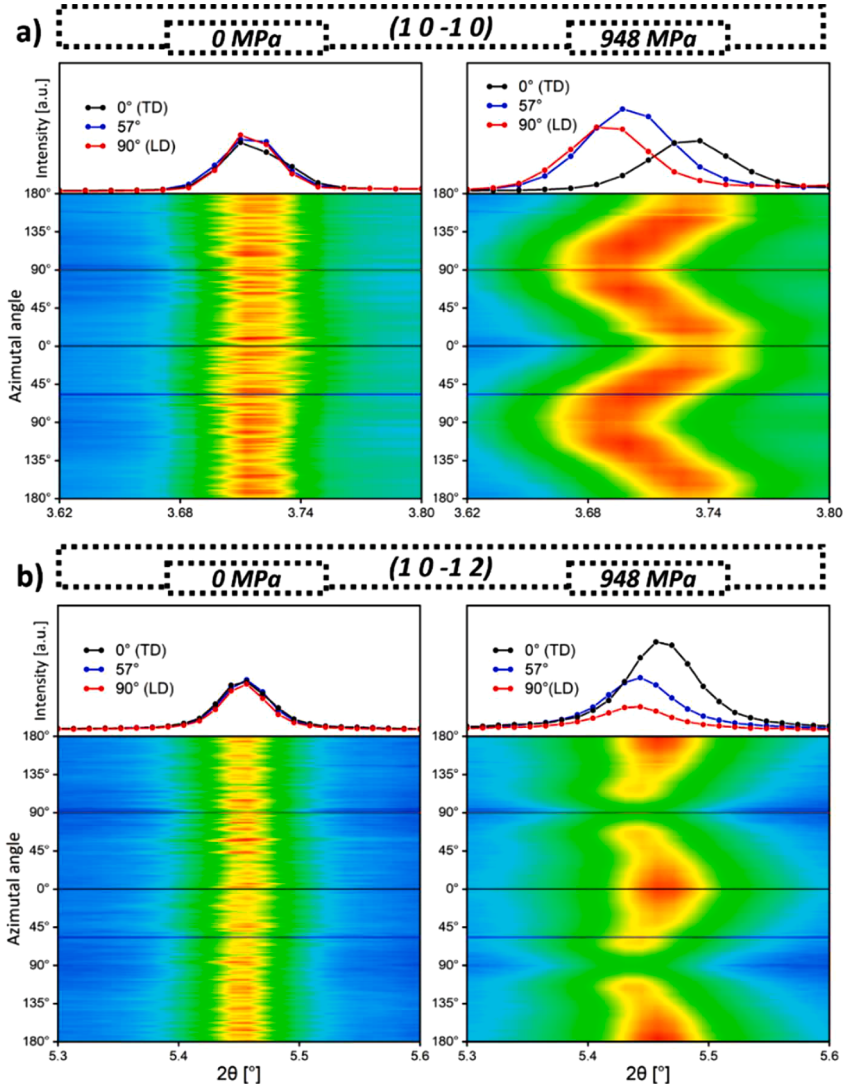
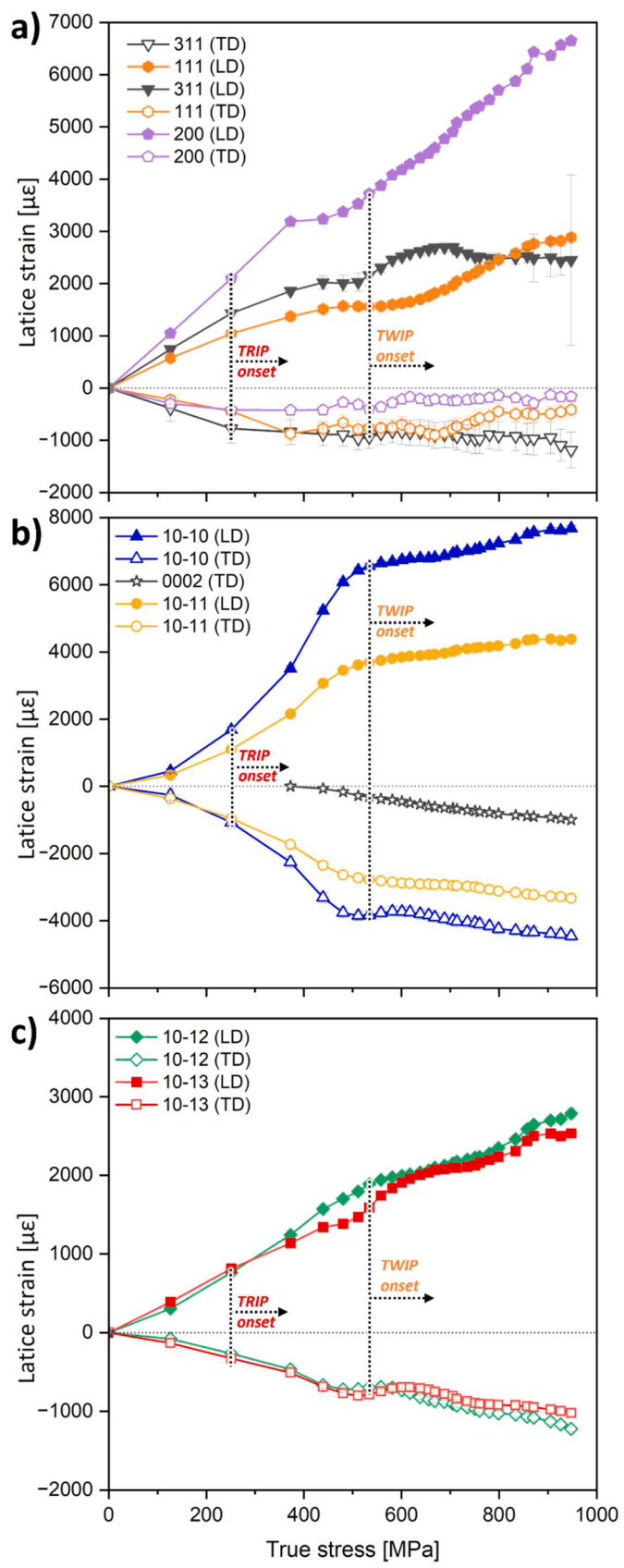


Fig. 6. Color maps corresponding to the stage I and IV of the tensile test on the: a) (1 0 -1 0) and b) (1 0 -1 2) diffraction peaks. This serves to evidence the different behavior exhibited by each peak upon the increase of stress and visible only by 1° cake integration of the diffraction patterns.



(caption on next page)

Fig. 7. Lattice strain evolution during tensile testing along TD and LD. (a) shows the evolution of γ -FCC (1 1 1), (2 0 0) and (3 1 1) diffraction peaks; (b) shows the evolution of ε -HCP (1 0 -1 0) and (1 0 -1 1) diffraction peaks. Here the (0 0 0 2) peak evolution is only shown for reference in the TD; (c) shows the evolution of ε -HCP (1 0 -1 2) and (1 0 -1 3) diffraction peaks.

Furthermore, considering the deformation mechanisms activated in the ε -HCP phase, besides the possibility for dislocation slip (discussed further ahead in this paper), literature (Fu et al., 2018; Li et al., 2017) shows that tensile {1 0 -1 2} <1 0 -1 0> and compression {1 0 -1 1} <1 0 -1 2> twinning modes are activated during deformation, corresponding to twinning misorientation angles of, approximately, 87° and 57° , respectively. Such phenomena can be analyzed through the peak intensity evolution during plastic deformation, where an abrupt splitting of intensity in the LD and TD evidences the inception of twinning (Fu et al., 2018; Shen et al., 2024).

With this in mind, Fig. 6 depicts color maps corresponding to stage I and IV of the tensile test on both the (1 0 -1 0) and (1 0 -1 2) diffraction peaks. Such allows us to evidence the different behavior exhibited by each peak, during the tensile test and highlight the effect that the tensile and compression twinning mode have on peak intensity and distribution.

Examining the integrated intensities evolution, it is possible to observe that the first twinning mode to occur is the {1 0 -1 2} <1 0 -1 0> tensile twinning mode at \approx 530 MPa. Such can be observed through the evolution of peak intensities on the LD and TD directions, on both the (1 0 -1 2) and (1 0 -1 3) reflections as exhibited in Fig. 4c). Such indicates the onset of the TWIP effect, where twining starts to take an important role in stress accommodation in the ε -HCP phase. It is also at this point that the (1 0 -1 1) reflection initiates a substantial increase in the LD, which, as mentioned by Fu et al. (Fu et al., 2018), can be attributed to the tensile twinning of the (1 0 -1 3) grains under the {1 0 -1 2} <1 0 -1 0> twinning mode. This is due to the fact that the lattice angle between the planes belonging to the (10-11) and (10-13) families of planes is approximately 90° and the twinning misorientation angle is \approx 87°, thus increasing the possibility for the (1 0 -1 3) grains to become oriented in the [1 0 -1 1] direction.

With further loading, the compression {1 0 -1 1} <1 0 -1 2> twinning mode is activated (at approximately 655 MPa). This can be noticed by the stabilization of the intensity behavior on the (1 0 -1 2) and (1 0 -1 0) diffraction peaks on the TD. Such results are coherent with the noticeable changes in the c/a ratio. Additionally, further analysis on this twining mode, which is not so evident, can be seen in Fig. 6, where the diffraction patterns corresponding to the beginning and end of the tensile test were integrated into 1° azimuthal angle segments, within the 2θ ranges corresponding to the (1 0 -1 0) and (1 0 -1 2) peaks.

Observing closely, prior to tensile testing (at 0 MPa condition) both diffraction peaks showcase an even distribution along the azimuthal angle, regarding their 2θ angle position. Nevertheless, a very different behavior can be seen at the final stages of the experiment. While the (1 0 -1 0) peak evidence a continuous distribution, reaching lower 2θ values at 90° (corresponding to the LD), it is also possible to observe that higher intensity values are obtained at 57° . Additionally, the (1 0 -1 2) peaks exhibit higher intensity values at 0° (corresponding to the TD) and also at 57° . In the latter case the 2θ angles are higher than those in the stress-free condition. Considering the behavior of (1 0 -1 0) diffraction reflection and the data acquired to this point it is viable to assume that the grains oriented in this direction tend to mainly exhibit dislocation slip as their main strain accommodation mechanism, finally exhibiting the compression twinning mode the last stages of the tensile test. As for the (1 0 -1 2) case, it is possible to infer that the increasing diffracted intensities due to tensile twinning result on a higher amount of (1 0 -1 2) oriented grains in the TD which tends to increase with the increasing stress, resulting in the compression of grains in this direction, which is perpendicular to loading. Such behavior then causes the compression twinning mode to activate, resulting in the higher (yet relatively lower) intensities oriented near the 57° azimuthal angle.

3.3. Lattice strain evolution upon loading

Having now established the phenomena associated with intensity changes, further information can be obtained by analyzing peak behavior in terms of their deviation from their stress-free 2θ position (at 0 MPa). Such was performed to unveil the strain effects (tensile or compression) on the LD and TD. Analyzing Fig. 7 permits us to observe that, as expected, the lattice strain behavior of all crystallographic planes deviates from linearity at \approx 250 MPa during the loading stage. In both γ -FCC and the ε -HCP cases, the DP-HEA exhibited a similar behavior to that expected from literature (Xu et al., 2020), where the highest magnitude for lattice strain was achieved at the final loading stages in both phases.

Additionally, for a full characterization of the lattice strain in each phase, the Young's modulus along the LD for each analyzed crystallographic plane, were calculated, and are summarized in Table 1.

Starting with the γ -FCC phase, Fig. 7(a) displays the lattice strain for the accessible diffraction peaks in both LD and TD. Comparably the largest lattice strain exhibited by the diffraction peaks can be observed in the direction of the tensile solicitation (LD).

Table 1

- Young's modulus and for different lattice planes of the constituent phases in the DP-HEA.

γ -FCC			
Reflection	(1 1 1)	(2 0 0)	(3 1 1)
E [GPa]	240.0 ± 13.7	119.6 ± 0.5	175.5 ± 3.3
ε -HCP			
Reflection	(1 0 -1 0)	(1 0 -1 1)	(1 0 -1 2)
E [GPa]	139.2 ± 37.3	217.0 ± 50.2	324.5 ± 38.5
			(1 0 -1 3)
			308.5 ± 8.9

The (2 0 0) diffraction peak exhibits the largest lattice strain in LD and the lowest in TD indicating its higher ductility when compared to the other reflections, while the (1 1 1) reflections exhibited the stiffest behavior.

For the ϵ -HCP lattice strain, the results are displayed in Fig. 7(b) and (c). Again, the (0 0 0 2) peak is shown here as a reference, as the data retrieved from it cannot be used to fully characterize its behavior on the ϵ -HCP phase. As expected, the lattice strain in the LD is higher than the TD. The (1 0 -1 0) exhibits the most ductile behavior, followed by the (1 0 -1 1), (1 0 -1 2) and the (1 0 -1 3) diffraction peaks. Furthermore, as the (1 0 -1 2) and (1 0 -1 3) peaks exhibit a continuously increasing trend in their lattice strain behavior, the (1 0 -1 0) and (1 0 -1 1) reflections start to exhibit a steady behavior when reaching the ≈ 530 MPa threshold, at the onset of tensile twinning marked as “TWIP onset”, showcasing their sensitivity to the onset of tensile twinning on the ϵ -HCP microstructure.

3.4. Dislocation density evolution with increasing load

With knowledge of the effect that TRIP and TWIP have on the accommodation of the imposed deformation, as seen in section 3.2, the activity of dislocation slip is still a major factor that can impact the strain accommodation on the DP-HEA. As such, assuming a direct relation between dislocation slip with dislocation density, it can be related to peak broadening (Shintani and Murata, 2011), whereas the results obtained by the Halder-Wagner method can aid in visualizing the increase in dislocation density in both phases during loading.

Fig. 8(a) displays the dislocation density evolution on the γ -FCC phase. Here a steady increase from $1.4 \times 10^{14} \text{ m}^{-2}$ to $8.2 \times 10^{14} \text{ m}^{-2}$ can be observed throughout the experiment. Such result allows us to conclude that the main strain accommodation mechanisms occurring in the γ -FCC phase are TRIP and dislocation slip.

However, the dislocation density progression on the ϵ -HCP phase allows us to observe the differences in dislocation slip behavior when the TWIP mechanism is activated through tensile and compression twinning of its grains. In this phase the dislocation density shown is calculated using the $b = 1/3 \langle 1 1 -2 0 \rangle$ and $b = 1/3 \langle 1 1 -2 3 \rangle$ burgers vectors, to define $\langle a \rangle$ and $\langle a + c \rangle$ dislocations, respectively. The difference between them allows us to observe that, although both dislocation slip types may occur in simultaneous, the $\langle a \rangle$ -mode is dominant over the $\langle a + c \rangle$ -mode, which makes sense provided that strain accommodation in the c-axis of the HCP unit cell can be attained thought twinning. Such behavior can be observed at the onset of the TWIP effect (roughly 530 MPa) where the values of dislocation density tend to exhibit a slower increase when compared to the dislocation density results calculated between the onset of TRIP and the activation of TWIP.

3.5. Phase load partitioning between γ -FCC and ϵ -HCP

The load imparted by each phase along with their averaged contribution is plotted against the true stress-true strain curve in Fig. 9(a). These results allow us to comprehend the stress partitioning occurring between both phases and their interaction to comply with the externally imposed stresses. Overall, a good agreement between the volume averaged curve, calculated by averaging the contribution of both phases with their corresponding volume fraction, and the true stress - true strain curve was obtained.

Here it is possible to observe that both phases yield at different stages. While the γ -FCC yields within the range of ≈ 250 MPa to ≈ 355 MPa of the true stress-true strain curve, the ϵ -HCP phase only deviates from linearity it when surpasses the ≈ 480 MPa threshold.

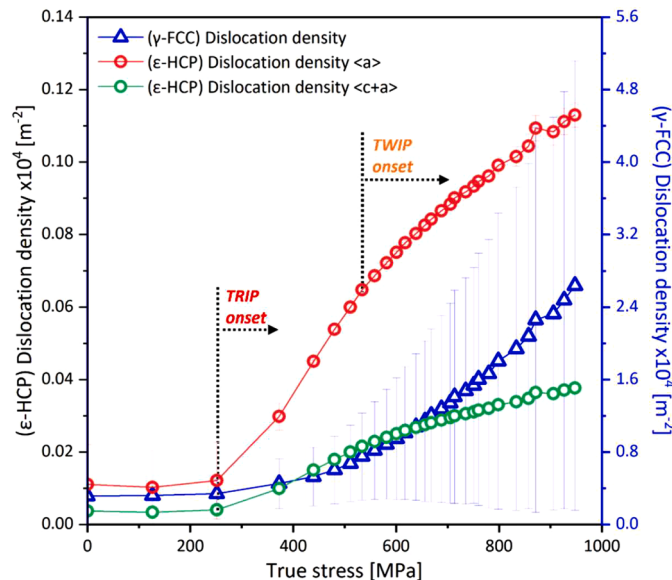


Fig. 8. Dislocation density evolution on the γ -FCC and ϵ -HCP phases, throughout the in-situ tensile experiment.

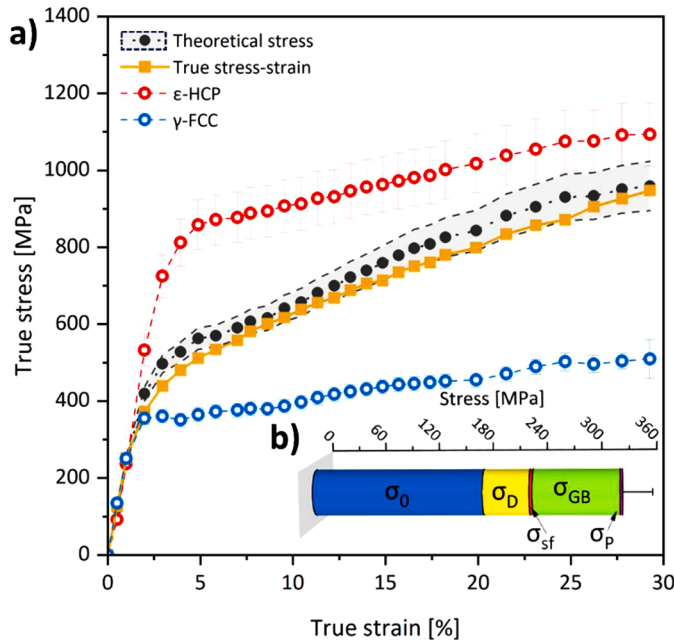


Fig. 9. (a) Load partitioning between the γ -FCC and ϵ -HCP phases. (b) Estimation of the yield strength of the DP-HEA based on the γ -FCC phase, which is the first phase to yield (σ_0 is the lattice friction stress, σ_D is the strengthening contribution from dislocations, σ_{SF} corresponds to the influence of staking faults and σ_{GB} represents the strengthening effect of grain boundaries).

Additionally, the calculated elastic modulus for the γ -FCC and ϵ -HCP phase were 170 ± 4 GPa and 222 ± 47 GPa, respectively. Calculation of the Poisson ratio was also considered, where the value of 0.33 ± 0.03 was obtained for the γ -FCC and 0.35 ± 0.08 was obtained for the ϵ -HCP phase. It is, therefore, possible to conclude that it is the γ -FCC phase that dictates the end of stage I of the tensile test, as marked in Fig. 2, meaning that once surpassing its yielding stress the TRIP effect activates, starting to actively transform the softer γ -FCC into the ϵ -HCP phase.

Calculation of the contributing factors to the yield strength of the γ -FCC phase was then performed to determine its yielding strength, and thus quantify the contribution factors that can contribute to the hastening/delay of the onset of stage II. In this regard, the load contribution to the γ -FCC phase yield strength was calculated based on using Eq. (8).

$$\sigma_y^{\gamma\text{-FCC}} = \sigma_0 + \sigma_D + \sigma_{SF} + \sigma_{GB} + \sigma_p \quad (8)$$

where σ_0 corresponds to the lattice friction stress (which is inherent from the material), σ_D is the strengthening contribution arising from dislocations, σ_{SF} corresponds to the influence of stacking faults, σ_{GB} represents the strengthening effect of grain boundaries and σ_p is strengthening contribution granted by the Mn oxides. Here, σ_0 was considered to be 179 MPa (Su et al., 2019), σ_D and σ_{GB} were calculated based on (Deng et al., 2021; Su et al., 2019) and σ_{SF} was obtained as in (Frank et al., 2020) (the equations are detailed in the supplementary material section). The results are shown in Fig. 9(b). These indicate that beyond σ_0 , which corresponds to the inherent strength of the DP-HEA, the grain boundary effect is the most impactful component, followed by the dislocation contribution and finally the stacking fault influence. At the same time the strengthening effect arising from the MnO particles can be considered negligible. Overall, the summed contribution renders in a yield stress value of 321 ± 31 MPa, which is coherent with the yielding stress range of the γ -FCC phase and the measured yield stress of the DP-HEA (319 MPa, as exhibited in Fig. 2c)).

Finally, with the impact of the in-situ tensile test reported using SXRD, we now delve into the interpretation of such results to unveil the complete mechanical response of the DP-HEA.

4. Discussion

Before we delve into the deformation behavior of the Fe₅₀Mn₃₀Co₁₀Cr₁₀ HEA under tensile testing, one important notion to establish is that of strain-induced martensitic transformation. This phenomenon occurs in certain materials, such as the present HEA, when they are subjected to mechanical deformation. Such effectively transforms an austenitic phase (in this case γ -FCC) into a martensitic one (ϵ -HCP). The martensitic phase is characterized by a different crystal structure, when compared to the phase that gives it its origin, granting the alloy unique mechanical properties, being at the core of the TRIP effect (Nishiyama et al., 1978).

Given the tensile nature of this study, the martensitic transformation occurring in this HEA, which exhibits both the TRIP and TWIP effects, allows for the continuous transformation of γ -FCC into ϵ -HCP, permitting the DP-HEA to benefit from the ductility and the strength associated with each phase.

Considering this, starting from the initial γ -FCC rich condition of the DP-HEA at 0 MPa (displayed in Fig. 4) there is a highly evident presence of ϵ -HCP (with a total volume phase fraction of 33 %). Conversely, this initial ϵ -HCP phase amount present within the microstructure can be described as thermal martensite, given that it is not related with mechanical loading, but manifests from the lattice defects developed during its manufacturing (Saboktakin Rizi et al., 2022) of such stacking faults leads to the formation of ϵ -HCP thin laths. Such thermally induced ϵ -HCP can then act as nuclei for the mechanically induced ϵ -HCP; thus, the initial phase volume fraction of ϵ -HCP is a parameter that directly influences the mechanical behavior of the alloy (Li et al., 2017, 2016; Liu et al., 2021; Lopes et al., 2023a).

With this matter established, direct comparison between Fig. 2c) and Fig. 9a), allows us to infer on both the macroscopic and phase specific behavior of the DP-HEA throughout the tensile test. This is especially relevant regarding the yielding stress of each phase. As mentioned, the yield stress of the material reaches ≈ 319 MPa, nevertheless, it is clear that the more ductile γ -FCC reaches its yielding stress earlier than the harder ϵ -HCP, dictating the onset of the TRIP effect and the macroscopic yield stress of the DP-HEA. Minding the yielding stress, Fig. 9b) indicates that beyond the inherent strength of the alloy, the influence of the grain boundaries stands as a major contribution, followed by dislocation density and with stacking faults exhibiting a minor effect on the yielding of the DP-HEA. Beyond this point, the load imparted by the DP-HEA is then distributed by each phase, where (obeying the rule of mixtures) the ϵ -HCP sustains higher stress levels, while a lower amount of stress is distributed towards the γ -FCC phase. This indicates that, while granting ductility to the DP-HEA, the most critical role of the γ -FCC phase is to enable the inception of ϵ -HCP in the microstructure, via the TRIP effect.

Furthermore, it is with focus set on the SXRD data that the succession of events occurring upon mechanical solicitation beyond the yielding stress can be unveiled and correlated. Accordingly, as a starting point for such interpretation, we divide the mechanical behavior of the alloy into four different loading stages. Each stage beginning at the, relatively precise, onset of each microstructural response to the external loading, more specifically regarding the TRIP and TWIP effects (refer to Fig. 10). For such, the stress ranges considered for marking the loading stages undertaken by the DP-HEA during tensile testing, are based on true stress values.

4.1. Stage I: from 0 MPa to ≈ 250 MPa

Given this, the stage I ranges from 0 MPa to the moment when the DP-HEA enters in the plastic regime. For analysis purposes we set the end of this stage at ≈ 250 MPa, which is the closest point to the yield stress within the elastic regime that was probed by SXRD.

This stage is mainly characterized by both phases being elastically deformed, so no influence of the TRIP or TWIP mechanisms on the mechanical response exist. The c/a ratio in this region shows a slight tendency to decrease, going from 1.6173 ± 0.0001 to 1.6170 ± 0.0002 . At this stage, the ϵ -HCP phase volume fraction and the corresponding dislocation density are stable, and the same can be said regarding the integrated peak intensity, in both the TD and LD. Nevertheless, the integrated peak intensity on the γ -FCC, tends to exhibit a small deviation from the initial values, indicating that the grains are rotating due to the imposed elastic strain. This preferential deformation of the γ -FCC phase is related to its lower strength compared to the ϵ -HCP phase.

Concerning the microstrain, however, it can be noted that it increases linearly in both directions, although exhibiting different slopes, which in turn reveals the stiffness associated with specific families of planes. Such is highlighted by the Young's modulus calculated and detailed in Table 1. Therefore, for the γ -FCC phase it can be observed that the (1 1 1) is the hardest and the (2 0 0) corresponds to the softest of the crystallographic plane families. Additionally, from the analyzed peaks of the ϵ -HCP phase it is revealed that (1 0 -1 0) corresponds to the softest family of planes, while the (1 0 -1 3) is the hardest. Such is coherent with the analyzed literature (Erdely et al., 2018; Fu et al., 2018; Shen et al., 2023). This is of particular interest to consider, given the anisotropic mechanical response of each family plane at later stages of loading. All things considered; this region exhibits the expected behavior of a material being deformed in the elastic range.

Moreover, the lattice strain of all peaks of both phases keeps increasing throughout the tensile test in both directions, especially in

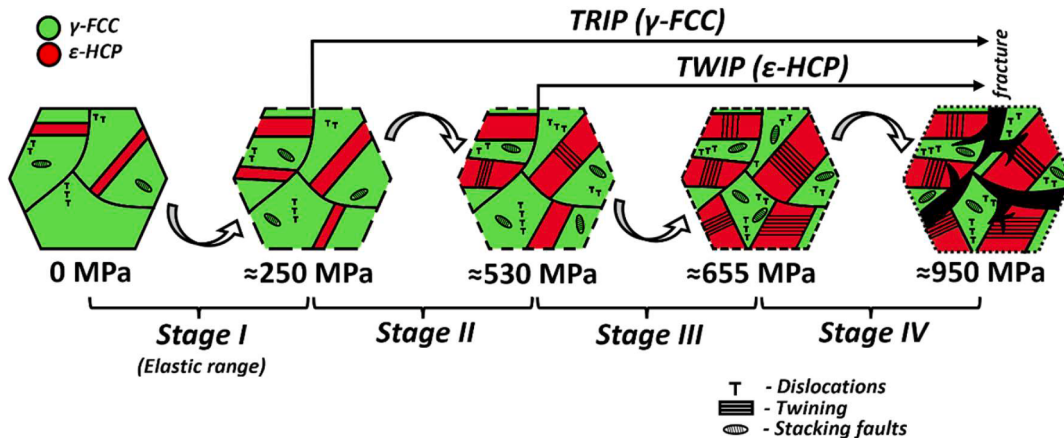


Fig. 10. Schematic representation of the loading stages undertaken by the DP-HEA, highlighting the stress thresholds for the activation of the multiple strain accommodation mechanisms developed upon tensile stress.

the LD (which is the direction of solicitation). Nevertheless, it is important to mention that each family of planes has its own pace and, with the increasing stress, will showcase their specific response, with this being accomplished by either TRIP, TWIP and/or dislocation slip. This way multiple mechanisms can act together to sustain the imposed loading.

Furthermore, although, at this stage, local plastic deformation can theoretically occur within the global elastic regime our SXRD analysis indicates no observable changes in phase fraction or peak parameters, likely due to the bulk analysis capabilities of this technique.

4.2. Stage II: from ≈ 250 MPa to ≈ 530 MPa

Upon the yielding of the γ -FCC phase, at ≈ 250 MPa, the beginning of a new stage can be marked up to the point where TWIP becomes a noticeable load bearing mechanism, via tensile twinning (at ≈ 530 MPa). At this stage, we can observe an increase on the ϵ -HCP phase volume fraction complemented with a sharp decrease on the overall hardening rate of the DP-HEA. This indicates that the activation of the TRIP effect acts as a major strain accommodating mechanism by granting the DP-HEA more strength as the stress level increases.

At this point of the tensile test, γ -FCC is still the dominant phase, thus the strain accommodation mechanisms beyond the evident TRIP effect, must also be analyzed. Evidently, in Fig. 8, the dislocation density on this phase exhibits a massive increase upon yielding, indicating that dislocation slip on γ -FCC also contributes to the overall accommodation of external stresses. Observing the intensities variations, however, it can be observed that no abrupt splitting of intensities in the LD and TD occurs. This leads to the conclusion that twinning is not a strain accommodation mechanism in the γ -FCC phase, as it would be expected from its ability to generate stacking faults.

Furthermore, a decrease in c/a ratio (reaching 1.6154 ± 0.0003) is also noticeable and can be related with dislocation slip modes on the ϵ -HCP. As mentioned by Bu et al. (Bu et al., 2019), the combined action of $\langle a \rangle$, $\langle c \rangle$ and $\langle a + c \rangle$ slip systems were observed via in-situ transmission electron microscopy in a Fe₅₀Mn₃₀Co₁₀Cr₁₀ HEA. This feature was attributed to a c/a ratio of 1.616 (which is lower than the ideal 1.633 value), highlighting that the reduction of the c/a ratio enhances the $\langle a + c \rangle$ slip activity in the DP-HEA. In the present case, the increasing dislocation density on the ϵ -HCP phase (refer to Fig. 8) calculated using both the basal and pyramidal Burgers vectors, indicates that both $\langle a \rangle$ and $\langle a + c \rangle$ type of dislocations show an massive increase at this stage of the tensile test, with the $\langle a \rangle$ -type being prevalent. In here, the steady evolution of integrated intensities also evidences grain rotation due to dislocation slip, owing to the lack of any sharp change in slope, which implies that deformation twinning is not the prevalent mechanism for strain accommodation.

4.3. Stage III: from ≈ 530 MPa to ≈ 655 MPa

Furthermore, the c/a ratio between ≈ 530 MPa and ≈ 655 MPa becomes stable, signaling the start of new deformation stage in the DP-HEA. The present results are in good agreement with those of Sinha et al. [17], since it is observed a stabilization of the c/a ratio when the relative volume fraction of each phase varies between 40 and 60%, which is correspondent to a range of externally applied stress of 530 to 655 MPa.

Being depended on the lattice parameters of the ϵ -HCP phase, the c/a ratio is, therefore, directly related to the volume variation induced by the TRIP effect, which inherently, requires the γ -FCC atoms to adapt in order to generate the ϵ -HCP basal plane and, perpendicularly to it, the c -axis of HCP unit cell, which requires the displacement of atoms from the neighboring lattice. Here, the stabilization of c/a ratio can be related to activation of twinning, provided that it is only responsible for the reorientation of a portion of the lattice, not resulting on the direct alteration of the lattice constants of a phase. Nevertheless, this phenomenon ultimately exerts more stresses in the γ -FCC phase, which then causes TRIP to occur more intensively, as it can be seen through the nucleation of new ϵ -HCP cells that will no longer be exposed to lower levels of stress.

This way, TWIP can be observed through the tensile twinning visible in the analyzed peaks intensities, although, interestingly, not all peaks showcase this effect at this stage. Such allows us to infer that, considering the crystallographic plane stiffness, noticeable by the lattice strain in the elastic range, the most rigid planes exhibit a sharp variation in intensity between the LD and TD (thus indicating tensile twinning), while the softer ones continue to accommodate strain via dislocation slip. This phenomenon is corroborated by the dislocation density evolution showcased by the $\langle a \rangle$ and $\langle a + c \rangle$ dislocation slip modes, where both have an evident decrease in slope, while the $\langle a \rangle$ -type, corresponding to basal slip, still increases in a relatively higher amount. Interestingly the effects of TWIP on the diffraction peak behavior can also be noticeable in the lattice strain variation of the ϵ -HCP phase, where the (1 0 -1 2) and (1 0 -1 3) peaks (corresponding to the stiffer crystallographic planes) continuously increase with the increasing stress, while the slopes on the lattice strain evolution of the softest peaks, (1 0 -1 0) and (1 0 -1 1), decreases. This evidences that TWIP is prevalent over dislocation slip in the ϵ -HCP phase, although not inhibiting it.

Regarding the integrated intensities analyzed in the γ -FCC phase, an overall decreasing trend for all peaks is depicted. Such is related to an increasing in the ϵ -HCP phase fraction, which at this point exhibits a sudden increase in slope. This allows us to conclude that when reaching the ≈ 530 MPa threshold, both TRIP, in the γ -FCC, and TWIP, in the ϵ -HCP, collaborate to achieve higher strengths and strains imparted by the DP-HEA. This combined behavior has an impact on the hardening rate, as during this stage the slope of the curve is decreasing, when the stress-strain curve reaches the corresponding stress levels, as visible in Fig. 2c). This indicates that the ability for these mechanisms to accommodate the increasing stress levels is decreasing, and so is the DP-HEA's capacity for hardening.

4.4. Stage IV: from \approx 655 MPa to \approx 950 MPa

Finally, when the stress-strain curve reaches \approx 655 MPa the hardening rate reaches a plateau. At this point the DP-HEA reaches the final last stage of the tensile test, which is marked by the onset of compression twinning.

Furthermore, the lattice strain keeps increasing at a coherent pace as the previous stage, however, the c/a ratio decreases which indicates that the $\langle a + c \rangle$ dislocation slip mode should become favored in supplementing the DP-HEA with strain accommodation in the ϵ -HCP c-axis (Bu et al., 2019). However, although the dislocation density curves of the ϵ -HCP keep increasing it does so at a lower rate. Such suggests that at this moment this dislocation slip mechanism is no longer the most effective way to allow for strain to be accommodated. The accommodation of strain is then accomplished by the increasing resolved compression stress in the TD, making it more energetically favorable (Frank et al., 2020; Mokdad et al., 2018).

This phenomenon can be seen in Fig. 6, where the intensity of both the dislocation slip prevalent (1 0 –1 0) peak and the tensile twinning affected (1 0 –1 2) peak, become noticeably high when oriented 57° from the TD direction, at the last analyzed point of the in-situ tensile test.

Regarding the γ -FCC phase (which is now under 30 % of the total phase volume fraction), the active strain accommodation mechanisms continue to be dislocation slip and the TRIP effect, according to decreasing γ -FCC volume fraction and increasing dislocation density.

Eventually, the sample fractured at \approx 950 MPa, corresponding to approximately 30% of engineering strain, marking the end of this stage and that of the in-situ tensile test.

5. Conclusions

In this work we contemplate the deformation behavior and microstructural evolution of a Fe₅₀Mn₃₀Co₁₀Cr₁₀ DP-HEA during in-situ tensile testing.

Quantitative analysis granted the analysis of the evolution of the continuously forming ϵ -HCP phase, upon yielding of the γ -FCC phase. Through this, mean ϵ -HCP volume fraction and c/a ratio evolution were assessed and calculation of diffraction peak-specific parameters were determined. Quantitative analysis was also performed to inspect the dislocation density evolution on both the major phases present in the DP-HEA.

Further investigation was conducted qualitatively, via single peak analysis. This allowed to observe the multiple mechanisms taking place to accommodate the externally imposed stress. In stage I, the DP-HEA deforms elastically until reaching the yielding stress of the soft γ -FCC phase, causing the onset of TRIP and the beginning of the stage II. This phenomenon occurs throughout the extent of the tensile test. As stress increases, strain accommodation on the ϵ -HCP phase causes the activation of the TWIP effect, which is noticeable by the onset of tensile twinning, visible through peak intensities. These two effects occur as dislocation slip takes place in both phases. Finally, stage IV occurs as compression twinning is activated until the eventual material fracture.

This sequence of events allowed to highlight the combination the transformative capability of γ -FCC (via TRIP) and the exceptional work hardening potential of ϵ -HCP (via TWIP).

CRediT authorship contribution statement

J.G. Lopes: Conceptualization, Methodology, Formal analysis, Investigation, Data curation, Writing – original draft, Writing – review & editing, Visualization. **J. Shen:** Methodology, Investigation, Formal analysis. **E. Maawad:** Resources, Investigation. **P. Agrawal:** Investigation. **N. Schell:** Resources, Investigation. **R.S. Mishra:** Investigation, Resources. **J.P. Oliveira:** Conceptualization, Methodology, Investigation, Writing – review & editing, Resources, Supervision, Project administration, Funding acquisition.

Declaration of competing interest

The authors declare that they have no known competing financial interests or personal relationships that could have appeared to influence the work reported in this paper.

Data availability

Data will be made available on request.

Acknowledgments

JGL, JS and JPO acknowledge Fundação para a Ciência e a Tecnologia (FCT - MCTES) for its financial support via the project UID/00667/2020 (UNIDEMI).

JGL acknowledges Fundação para a Ciência e a Tecnologia (FCT - MCTES) for funding the Ph.D. Grant 2020.07350.BD.

JS and JPO acknowledge the funding by national funds from FCT - Fundação para a Ciência e a Tecnologia, I.P., in the scope of the projects LA/P/0037/2020, UIDP/50025/2020 and UIDB/50025/2020 of the Associate Laboratory Institute of Nanostructures, Nanomodelling and Nanofabrication – i3N.

The authors acknowledge DESY (Hamburg, Germany), a member of the Helmholtz Association HGF, for the provision of experimental facilities. Beamtime was allocated for proposal I-20211528 EC. The research leading to this result has been supported by the project CALIPSOplus under the Grant Agreement 730872 from the EU Framework Programme for Research and Innovation HORIZON 2020.

Supplementary materials

Supplementary material associated with this article can be found, in the online version, at [doi:10.1016/j.ijplas.2024.104048](https://doi.org/10.1016/j.ijplas.2024.104048).

References

- Abdolvand, H., Majkut, M., Oddershede, J., Schmidt, S., Lienert, U., Diak, B.J., Withers, P.J., Daymond, M.R., 2015. On the deformation twinning of Mg AZ31B: a three-dimensional synchrotron X-ray diffraction experiment and crystal plasticity finite element model. *Int. J. Plast.* 70, 77–97. <https://doi.org/10.1016/j.ijplas.2015.03.001>.
- Bahramyan, M., Mousavian, R.T., Brabazon, D., 2020. Study of the plastic deformation mechanism of TRIP-TWIP high entropy alloys at the atomic level. *Int. J. Plast.* 127, 102649. <https://doi.org/10.1016/j.ijplas.2019.102649>.
- Basu, S., Li, Z., Pradeep, K.G., Raabe, D., 2018. Strain rate sensitivity of a TRIP-assisted dual-phase high-entropy alloy. *Front. Mater.* 5, 30. <https://doi.org/10.3389/fmats.2018.00030>.
- Bu, Y., Li, Z., Liu, J., Wang, H., Raabe, D., Yang, W., 2019. Nonbasal slip systems enable a strong and ductile hexagonal-close-packed high-entropy phase. *Phys. Rev. Lett.* 122, 075502 <https://doi.org/10.1103/PHYSREVLETT.122.075502>.
- Clayton, J.D., Lloyd, J.T., 2021. A dynamic finite-deformation constitutive model for steels undergoing slip, twinning, and phase changes. *J. Dynam. Behav. Mater.* 7, 217–247. <https://doi.org/10.1007/s40870-020-00279-z>.
- Deng, H.W., Wang, M.M., Xie, Z.M., Zhang, T., Wang, X.P., Fang, Q.F., Xiong, Y., 2021. Enhancement of strength and ductility in non-equiautomatic CoCrNi medium-entropy alloy at room temperature via transformation-induced plasticity. *Mater. Sci. Engineer.: A* 804, 140516. <https://doi.org/10.1016/J.MSEA.2020.140516>.
- Ding, Hao, Ding, Hua, Song, D., Tang, Z., Yang, P., 2011. Strain hardening behavior of a TRIP/TWIP steel with 18.8% Mn. *Mater. Sci. Engineer.: A* 528, 868–873. <https://doi.org/10.1016/J.MSEA.2010.10.040>.
- Ellyson, B., Saville, A., Fezzaa, K., Sun, T., Parab, N., Finfrock, C., Rietema, C.J., Smith, D., Copley, J., Johnson, C., Becker, C.G., Klemm-Toole, J., Kirk, C., Kedir, N., Gao, J., Chen, W., Clarke, K.D., Clarke, A.J., 2023. High strain rate deformation of aged TRIP Ti-10V-2Fe-3Al (wt.%) examined by in-situ synchrotron X-ray diffraction. *Acta Mater.* 245, 118621. <https://doi.org/10.1016/j.actamat.2022.118621>.
- Erdely, P., Staron, P., Maawad, E., Schell, N., Clemens, H., Mayer, S., 2018. Lattice and phase strain evolution during tensile loading of an intermetallic, multi-phase γ -TiAl based alloy. *Acta Mater.* 158, 193–205. <https://doi.org/10.1016/J.ACTAMAT.2018.07.062>.
- Ferreri, N.C., Feng, Z., Savage, D.J., Brown, D.W., Clausen, B., Sisneros, T.A., Knezevic, M., 2022. In-situ high-energy X-ray diffraction and crystal plasticity modeling to predict the evolution of texture, twinning, lattice strains and strength during loading and relo5d4wading of beryllium. *Int J Plast* 150, 103217. <https://doi.org/10.1016/j.ijplas.2022.103217>.
- Frank, M., Nene, S.S., Chen, Y., Gwalani, B., Kautz, E.J., Devaraj, A., An, K., Mishra, R.S., 2020. Correlating work hardening with co-activation of stacking fault strengthening and transformation in a high entropy alloy using in-situ neutron diffraction. *Sci. Rep.* 10 (1), 1–10. <https://doi.org/10.1038/s41598-020-79492-8>, 202010.
- Fu, S., Bei, H., Chen, Y., Liu, T.K., Yu, D., An, K., 2018. Deformation mechanisms and work-hardening behavior of transformation-induced plasticity high entropy alloys by in -situ neutron diffraction. *Mater. Res. Lett.* 6, 620–626. <https://doi.org/10.1080/21663831.2018.1523239>.
- George, E.P., Raabe, D., Ritchie, R.O., 2019. High-entropy alloys. *Nat. Rev. Mater.* 4 (8), 515–534. <https://doi.org/10.1038/s41578-019-0121-4>, 20194.
- Grässel, O., Krüger, L., Frommeyer, G., Meyer, L.W., 2000. High strength Fe-Mn-(Al, Si) TRIP/TWIP steels development — Properties — Application. *Int. J. Plast.* 16, 1391–1409. [https://doi.org/10.1016/S0749-6419\(00\)00015-2](https://doi.org/10.1016/S0749-6419(00)00015-2).
- Gui, Y., An, D., Han, F., Lu, X., Kang, G., Zhang, X., 2022. Multiple-mechanism and microstructure-based crystal plasticity modeling for cyclic shear deformation of TRIP steel. *Int. J. Mech. Sci.* 222, 107269 <https://doi.org/10.1016/J.IJMECSCI.2022.107269>.
- He, B.B., 2018. Two-dimensional X-ray Diffraction. Wiley. <https://doi.org/10.1002/9781119356080>.
- He, Z.F., Jia, N., Wang, H.W., Liu, Y., Li, D.Y., Shen, Y.F., 2020. The effect of strain rate on mechanical properties and microstructure of a metastable FeMnCoCr high entropy alloy. *Mater. Sci. Engineer.: A* 776, 138982. <https://doi.org/10.1016/J.MSEA.2020.138982>.
- Hilhorst, A., Jacques, P.J., Pardoën, T., 2023. Towards the best strength, ductility, and toughness combination: high entropy alloys are excellent, stainless steels are exceptional. *Acta Mater.* 260, 119280. <https://doi.org/10.1016/j.actamat.2023.119280>.
- Hossain, A.M., Kumar, N., 2022. Microstructure and mechanical properties of a dual phase transformation induced plasticity Fe-Mn-Co-Cr high entropy alloy. *J. Alloys Compd.* 893, 162152 <https://doi.org/10.1016/J.JALCOM.2021.162152>.
- Hull, D., Bacon, D.J., 2011. Introduction to dislocations, Fifth Edition. Intro. Dislocat. 1–257. <https://doi.org/10.1016/C2009-0-64358-0>, Fifth Edition.
- Kieffer, J., Valls, V., Blanc, N., Hennig, C., 2020. New tools for calibrating diffraction setups. urn:nbn:de:hbz:5:1-s1600577520000776.
- Kim, J.-K., Kim, J.H., Park, H., Kim, J.-S., Yang, G., Kim, R., Song, T., Suh, D.-W., Kim, J., 2022. Temperature-dependent universal dislocation structures and transition of plasticity enhancing mechanisms of the Fe40Mn40Co10Cr10 high entropy alloy. *Int. J. Plast.* 148, 103148 <https://doi.org/10.1016/j.ijplas.2021.103148>.
- Lai, Q., Yang, H., Wei, Y., Zhou, H., Xiao, L., Ying, H., Lan, S., You, Z., Kou, Z., Feng, T., Lu, Q., Jacques, P., Pardoën, T., 2022. Transformation plasticity in high strength, ductile ultrafine-grained FeMn alloy processed by heavy ausforming. *Int. J. Plast.* 148, 103151 <https://doi.org/10.1016/j.ijplas.2021.103151>.
- Langford, J.I., 1978. A rapid method for analysing the breadths of diffraction and spectral lines using the voigt function. *J. Appl. Cryst.* 11, 10–14.
- Lavakumar, A., Sarangi, S.S., Chilla, V., Narsimhachary, D., Ray, R.K., 2021. A “new” empirical equation to describe the strain hardening behavior of steels and other metallic materials. *Mater. Sci. Engineer.: A* 802, 140641. <https://doi.org/10.1016/J.MSEA.2020.140641>.
- Li, H., Liu, Y., Zhao, W., Liu, B., Tominaga, A., Shobu, T., Wei, D., 2023a. Deformation mechanism of a strong and ductile maraging steel investigated using in-situ X-ray synchrotron diffraction. *Int. J. Plast.* 165, 103612 <https://doi.org/10.1016/j.ijplas.2023.103612>.
- Li, Y.X., Nutor, R.K., Zhao, Q.K., Zhang, X.P., Cao, Q.P., Sohn, S.S., Wang, X.D., Ding, S.Q., Zhang, D.X., Zhou, H.F., Wang, J.W., Jiang, J.Z., 2023b. Unraveling the deformation behavior of the Fe45Co25Ni10V20 high entropy alloy. *Int. J. Plast.* 165, 103619 <https://doi.org/10.1016/j.ijplas.2023.103619>.
- Li, Y.Z., Liang, Z.Y., Huang, M.X., 2022. Strengthening contributions of dislocations and twins in warm-rolled TWIP steels. *Int. J. Plast.* 150, 103198 <https://doi.org/10.1016/j.ijplas.2021.103198>.
- Li, Z., Pradeep, K.G., Deng, Y., Raabe, D., Tasan, C.C., 2016. Metastable high-entropy dual-phase alloys overcome the strength–ductility trade-off. *Nature* 534 (7606), 227–230. <https://doi.org/10.1038/nature17981>, 2016534.
- Li, Z., Tasan, C.C., Pradeep, K.G., Raabe, D., 2017. A TRIP-assisted dual-phase high-entropy alloy: grain size and phase fraction effects on deformation behavior. *Acta Mater.* 131, 323–335. <https://doi.org/10.1016/J.ACTAMAT.2017.03.069>.
- Lin, Y., Wu, B., Li, S., Mao, S., Liu, X., Zhang, Y., Wang, L., 2015. The quantitative relationship between microstructure and mechanical property of a melt spun Al–Mg alloy. *Mater. Sci. Engineer.: A* 621, 212–217. <https://doi.org/10.1016/J.MSEA.2014.10.047>.

- Liu, Y., Tu, J., Deng, L., Wang, C.hao, Zhou, Z.ming, Jiang, Z.tao, Luo, J.ru, 2021. Characteristics of thermal- and strain-induced ϵ -martensite in Fe50Mn30Co10Cr10 multi-component alloy: effect of grain size. *Mater. Charact.* 171, 110817. <https://doi.org/10.1016/J.MATCHAR.2020.110817>.
- Lopes, J.G., Agrawal, P., Shen, J., Schell, N., Mishra, R.S., Oliveira, J.P., 2023a. Evolution of microstructure and mechanical properties in gas tungsten arc welded dual-phase Fe50Mn30Co10Cr10 high entropy alloy. *Mater. Sci. Engineer.: A* 878, 145233. <https://doi.org/10.1016/J.MSEA.2023.145233>.
- Lopes, J.G., Rocha, P., Santana, D.A., Shen, J., Maawad, E., Schell, N., Courty, F.G., Oliveira, J.P., 2023b. Impact of arc-based welding on the microstructure evolution and mechanical properties in newly developed Cr29.7Co29.7Ni35.4Al4Ti1.2 multi-principal element alloy. *Adv. Eng. Mater.* 25, 2300109. <https://doi.org/10.1002/ADEM.202300109>.
- Ma, L., Wang, L., Nie, Z., Wang, F., Xue, Y., Zhou, J., Cao, T., Wang, Y., Ren, Y., 2017. Reversible deformation-induced martensitic transformation in Al0.6CoCrFeNi high-entropy alloy investigated by in situ synchrotron-based high-energy X-ray diffraction. *Acta Mater.* 128, 12–21. <https://doi.org/10.1016/J.ACTAMAT.2017.02.014>.
- Magagnosc, D.J., Field, D.M., Meredith, C.S., Walter, T.R., Limmer, K.R., Lloyd, J.T., 2021. Superior strength and ductility in a low density duplex steel studied by in situ neutron diffraction. *Mater. Sci. Engineer.: A* 799, 140252. <https://doi.org/10.1016/J.MSEA.2020.140252>.
- Miracle, D.B., Senkov, O.N., 2017. A critical review of high entropy alloys and related concepts. *Acta Mater.* 122, 448–511. <https://doi.org/10.1016/j.actamat.2016.08.081>.
- Mokdad, F., Chen, D.L., Li, D.Y., 2018. Twin-twin interactions and contraction twin formation in an extruded magnesium alloy subjected to an alteration of compressive direction. *J. Alloys Compd.* 737, 549–560. <https://doi.org/10.1016/J.JALLCOM.2017.12.043>.
- Naeem, M., He, H., Harjo, S., Kawasaki, T., Zhang, F., Wang, B., Lan, S., Wu, Z., Wu, Y., Lu, Z., Liu, C.T., Wang, X.L., 2020. Extremely high dislocation density and deformation pathway of CrMnFeCoNi high entropy alloy at ultralow temperature. *Scr. Mater.* 188, 21–25. <https://doi.org/10.1016/J.SCRIPTAMAT.2020.07.004>.
- Nishiyama, Z., Fine, M.E., Meshii, M., Wayman, C.M., 1978. *Martensitic Transformation*. Academic Press.
- Peng, B., Jie, J., Liu, J., Qu, J., Wang, M., Sun, J., Chen, X., Ren, Z., Li, T., 2022. Synergistic strengthening of heterogeneous interface far beyond rule of mixture in Cu/1010 steel bimetal laminar composite. *Mater. Sci. Engineer.: A* 851, 143609. <https://doi.org/10.1016/J.MSEA.2022.143609>.
- Rogachev, A.S., Kovalev, D.Y., Kochetov, N.A., Shchukin, A.S., Vadchenko, S.G., 2021. Evolution of crystal structure in high-entropy AlCoCrFeNi alloy: an in situ high-temperature X-ray diffraction study. *J. Alloys Compd.* 861, 158562. <https://doi.org/10.1016/J.JALLCOM.2020.158562>.
- Saboktakin Rizi, M., Minouei, H., Lee, B.J., Toroghinejad, M.R., Hong, S.I., 2022. Effects of carbon and molybdenum on the nanostructural evolution and strength/ductility trade-off in Fe40Mn40Co10Cr10 high-entropy alloys. *J. Alloys Compd.* 911, 165108. <https://doi.org/10.1016/J.JALLCOM.2022.165108>.
- Saville, A.I., Creuziger, A., Mitchell, E.B., Vogel, S.C., Benzing, J.T., Klemm-Toole, J., Clarke, K.D., Clarke, A.J., 2021. MAUD rietveld refinement software for neutron diffraction texture studies of single- and dual-phase materials. *Integr. Mater. Innov.* 10, 461–487. <https://doi.org/10.1007/s40192-021-00224-5>.
- Shen, J., Lopes, J.G., Zeng, Z., Choi, Y.T., Maawad, E., Schell, N., Kim, H.S., Mishra, R.S., Oliveira, J.P., 2023. Deformation behavior and strengthening effects of an eutectic AlCoCrFeNi2.1 high entropy alloy probed by in-situ synchrotron X-ray diffraction and post-mortem EBSD. *Mater. Sci. Engineer.: A* 872, 144946. <https://doi.org/10.1016/J.MSEA.2023.144946>.
- Shen, J., Zhang, W., Lopes, J.G., Pei, Y., Zeng, Z., Maawad, E., Schell, N., Baptista, A.C., Mishra, R.S., Oliveira, J.P., 2024. Evolution of microstructure and deformation mechanisms in a metastable Fe42Mn28Co10Cr15Si5 high entropy alloy: a combined in-situ synchrotron X-ray diffraction and EBSD analysis. *Mater. Des.* 238, 112662. <https://doi.org/10.1016/j.matdes.2024.112662>.
- Shintani, T., Murata, Y., 2011. Evaluation of the dislocation density and dislocation character in cold rolled Type 304 steel determined by profile analysis of X-ray diffraction. *Acta Mater.* 59, 4314–4322. <https://doi.org/10.1016/J.ACTAMAT.2011.03.055>.
- Sinha, S., Nene, S.S., Frank, M., Liu, K., Agrawal, P., Mishra, R.S., 2019. On the evolving nature of c/a ratio in a hexagonal close-packed epsilon martensite phase in transformative high entropy alloys. *Sci. Rep.* 9 (1), 1–14. <https://doi.org/10.1038/s41598-019-49904-5>, 2019.
- Smallman, R.E., Westmacott, K.H., 1957. Stacking faults in face-centred cubic metals and alloys. *Philosoph. Magaz.* 2, 669–683. <https://doi.org/10.1080/14786435708242709>.
- Sohrabi, M.J., Mirzadeh, H., Sadeghpour, S., Mahmudi, R., 2023. Grain size dependent mechanical behavior and TRIP effect in a metastable austenitic stainless steel. *Int. J. Plast.* 160, 103502. <https://doi.org/10.1016/j.ijplas.2022.103502>.
- Su, J., Raabe, D., Li, Z., 2019. Hierarchical microstructure design to tune the mechanical behavior of an interstitial TRIP-TWIP high-entropy alloy. *Acta Mater.* 163, 40–54. <https://doi.org/10.1016/J.ACTAMAT.2018.10.017>.
- Tang, Y., Wang, R., Xiao, B., Zhang, Z., Li, S., Qiao, J., Bai, S., Zhang, Y., Liaw, P.K., 2023. A review on the dynamic-mechanical behaviors of high-entropy alloys. *Prog. Mater. Sci.* 135, 101090. <https://doi.org/10.1016/j.jmatsci.2023.101090>.
- Verma, R., Jayaganthan, R., Nath, S.K., Srinivasan, A., 2020. Effect of multiaxial forging followed by hot rolling on non-basal planes and its influence on tensile and fracture toughness behaviour of Mg–4Zn–4Gd alloy. *Mater. Sci. Engineer.: A* 774, 138890. <https://doi.org/10.1016/J.MSEA.2019.138890>.
- Wang, J., Ferdowsi, M.R.G., Kada, S.R., Lynch, P.A., Wang, Z., Kimpton, J.A., Barnett, M.R., 2021. Stress relaxations during cyclic loading-unloading in precipitation hardened Mg–4Zn. *Acta Mater.* 205, 116531. <https://doi.org/10.1016/J.ACTAMAT.2020.116531>.
- Wong, S.L., Madivala, M., Prahl, U., Roters, F., Raabe, D., 2016. A crystal plasticity model for twinning- and transformation-induced plasticity. *Acta Mater.* 118, 140–151. <https://doi.org/10.1016/J.ACTAMAT.2016.07.032>.
- Xu, N., Li, S., Li, R., Zhang, M., Yan, Z., Cao, Y., Nie, Z., Ren, Y., Wang, Y.D., 2020. In situ investigation of the deformation behaviors of Fe20Co30Cr25Ni25 and Fe20Co30Cr30Ni20 high entropy alloys by high-energy X-ray diffraction. *Mater. Sci. Engineer.: A* 795, 139936. <https://doi.org/10.1016/J.MSEA.2020.139936>.
- Ye, Y.F., Wang, Q., Lu, J., Liu, C.T., Yang, Y., 2016. High-entropy alloy: challenges and prospects. *Mater. Tod.* 19, 349–362. <https://doi.org/10.1016/J.MATTOD.2015.11.026>.
- Zeng, Z., Zhou, M., Lynch, P., Mompiou, F., Gu, Q., Esmaily, M., Yan, Y., Qiu, Y., Xu, S., Fujii, H., Davies, C., Nie, J.F., Birbilis, N., 2021. Deformation modes during room temperature tension of fine-grained pure magnesium. *Acta Mater.* 206, 116648. <https://doi.org/10.1016/J.ACTAMAT.2021.116648>.
- Zhao, G., Li, X., Petrinic, N., 2021. Materials information and mechanical response of TRIP/TWIP Ti alloys. *NPJ Computational Materials* 7 (1), 1–9. <https://doi.org/10.1038/s41524-021-00560-2>, 2021.